Quantitative Structure-Based Prediction of Electron Spin Decoherence in Organic Radicals]

Supporting Information

Elizabeth R. Canarie, Samuel M. Jahn, Stefan Stoll

Department of Chemistry, University of Washington, Seattle, Washington 98195, United States

Table of Contents

1. Materials and Methods

1.1 Samples

2,2,6,6-tetramethylpiperidine-1-oxyl (TEMPO) was obtained from Sigma-Aldrich; 2,2,6,6,-tetramethylpiperidine-d_{18}-1-oxyl (d_{18}-TEMPO) from CDN Isotopes; and the trityl radical p_1TAM was synthesized at West Virginia University as previously described.[1]

Samples were prepared in 1:1 (w:w) H_2O:glycerol (corresponding to 16% molar fraction glycerol). This solvent composition was selected to minimize any effects from solute aggregation on decoherence. Measured phase memory times are shown in Figure S1. Samples with lower glycerol concentrations show shortened echo decays, whereas increasing glycerol concentrations beyond 1:1 (w:w) did not significantly affect the echo decay rate.

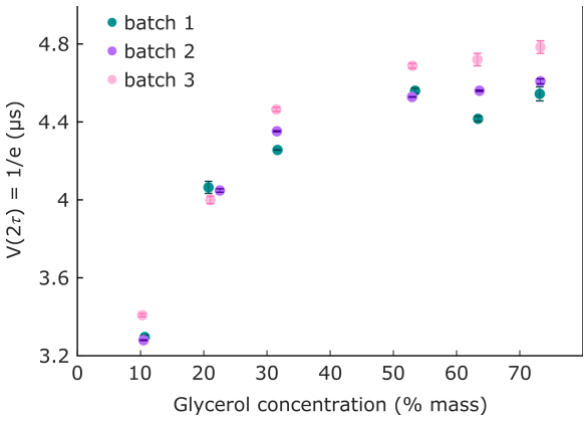

Figure S1. Plot of measured phase memory time as a function of glycerol concentration (% mass) in a 200 μM TEMPO sample. The phase memory time is defined as the point at which the signal intensity decays to 1/e of its original intensity. The three batches represent three independently prepared samples at each glycerol concentration.

The sample concentrations were approximately 10 μM (p_1TAM), 100 μM (d_{18}-TEMPO), and 200 μM (TEMPO). They were chosen to minimize decoherence effects from instantaneous diffusion (ID),[2] which is described by an exponential decay with decay time t_{ID} given by[3]

$$t_{\mathrm{ID}} = \left(\frac{4\pi^2}{9\sqrt{3}}\frac{\mu_0}{4\pi}\hbar\gamma_e^2\eta c\right)^{-1} \tag{S1}$$

with the concentration c (in spins/m^3) and the excitation efficiency η. Estimating $\eta \approx 0.25$ for TEMPO, this gives t_{ID} of 80 μs for 100 μM, and 40 μs for 200 μM. Estimating $\eta \approx 1$ for p_1TAM, this gives t_{ID} of 200 μs for 10 μM. All these times are significantly longer than the experimentally observed time scales (4-5 μM).

For measurements at Q-band, 30-50 μL of sample were syringed into 1.50 mm O.D. 1.1 mm I.D. quartz tubes (Sutter Instrument). For the X-band measurement shown in the SI, ca. 100 μL of sample was syringed into a 4 mm O.D. 3 mm I.D. quartz tube (Wilmad-LabGlass). The samples were snap frozen in liquid nitrogen over approximately 10 seconds while gently shaking the tube submerged into the nitrogen. The samples were visually good optical glasses.

1.2 Measurements

The Q-band experiments (ca. 33.8 GHz, 1.2 T) were performed on a Bruker Elexsys E580 spectrometer equipped with a Bruker D2 dielectric resonator. The microwave power was amplified with a 300 W Applied Systems Engineering TWT amplifier. The X-band experiment on d_{18}-TEMPO (ca. 9.6 GHz, 0.34 T) was performed on the same spectrometer utilizing a Bruker MD4 dielectric resonator and a 1 kW Applied Systems Engineering TWT amplifier.

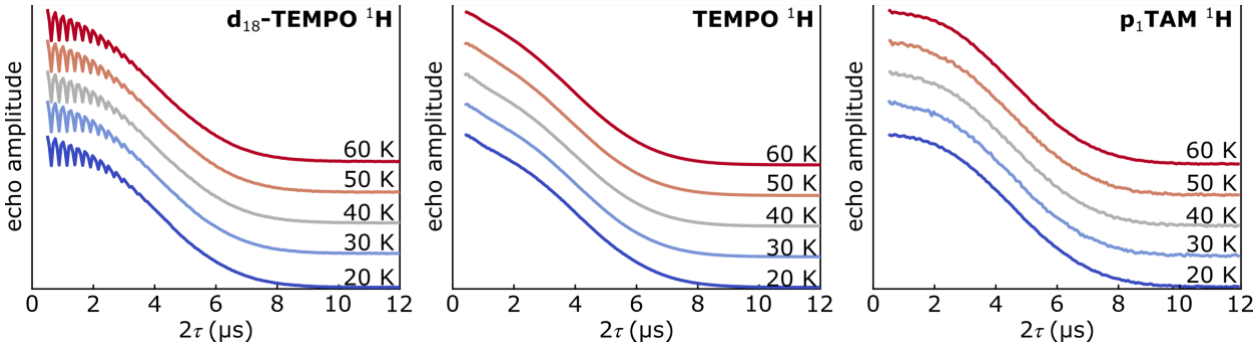

Figure S2. Q-band echo decay experiments from 20-60 K. From left to right, 100 μM d_{18}-TEMPO, 200 μM TEMPO, and approximately 10 μM p_1TAM, all in 1:1 (w:w) H_2O:glycerol. All data are scaled to identical amplitudes at the start point.

The measurements were conducted at the field values that gave the maximum echo amplitudes. Optimal pulse lengths were determined from the minimum of the nutation signal observed in a Rabi nutation experiment. At Q-band, the π/2 and π pulses for d_{18}-TEMPO, TEMPO, and p_1TAM were: 10/20 ns, 26/52 ns, and 14/28 ns, respectively. For the X-band experiment on d_{18}-TEMPO, π/2 and π pulses of 14/28 ns were used. The shot repetition times were sample and temperature dependent and were determined by increasing the value of the shot repetition time until there was no further change in recorded echo intensity, in order to avoid saturation effects. For experiments at 20 K, typical shot repetition times were on the order of 700 ms to 1 s. Hahn echo decays were performed with the pulse sequence $\pi/2 - \tau - \pi - \tau - echo$ by varying τ. The minimum τ value was 250 ns for d_{18}-TEMPO and p_1TAM and 200 ns for TEMPO. The minimum τ value for the X-band d_{18}-TEMPO experiment was 400 ns. The maximum τ was chosen to capture the entire echo decay, until the echo decays to essentially zero.

2. Temperature dependence

To identify any possible contributions to decoherence from thermal molecular motions and spin-lattice relaxation mechanisms, Q-band experiments were performed from 20-60 K in increments of 10 K (Figure S2). The decays are were fit using MATLAB's cftool with a stretched exponential (SE) of the form

$$V_{\mathrm{SE}}(2\tau) = V_0 \cdot \exp\left(-\left(\frac{2\tau}{T_{\mathrm{M}}}\right)^{x}\right), \tag{S2}$$

where V_0 is the echo amplitude at time $2\tau = 0$; T_{M} is the phase memory time; and x is the stretching exponent. For TEMPONE in frozen methyl-free solvents, the stretching exponent was previously found to be between 2 and 2.5.[4] A single stretched exponential was sufficient to capture the shape and timescale of the echo decays for d_{18}-TEMPO and p_1TAM. There are additional components in the decays of the TEMPO sample.

To phenomenologically account for the components present in the TEMPO experiments, the data were also fit with a sum of two stretched exponentials (SSE) and a product of two stretched exponentials (PSE).

$$V_{\mathrm{SSE}}(2\tau) = V_{0,1} \cdot \exp\left(-\left(\frac{2\tau}{T_{\mathrm{M},1}}\right)^{x_1}\right) + V_{0,2} \cdot \exp\left(-\left(\frac{2\tau}{T_{\mathrm{M},2}}\right)^{x_2}\right). \tag{S3}$$

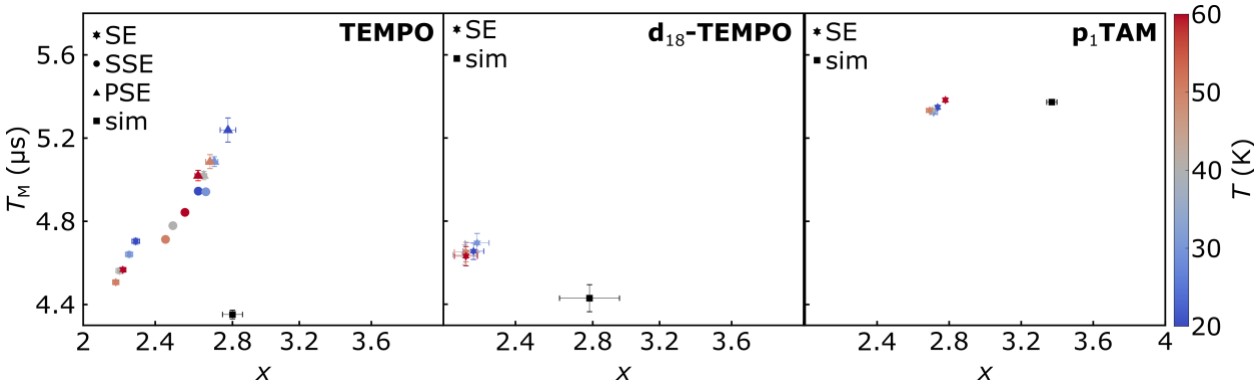

Figure S3. Plots of x versus T_M from fit to the data in Fig. S2. From left to right: TEMPO, d_{18}-TEMPO, and p_1TAM. Both d_{18}-TEMPO (middle) and p_1TAM (right) are fit well with a stretched exponential (SE). TEMPO (left) requires an additional component to fit the data, so the parameters from a sum of stretched exponentials (SSE) and product of stretched exponentials (PSE) are shown in addition to the SE parameters. The simulation parameters are shown as a square. The simulation values were obtained by fitting a stretched exponential to the simulation and extracting x and T_M values from the fit.

$$V_{\mathrm{PSE}}(2\tau) = V_{0,1} \cdot \exp\left(-\left(\frac{2\tau}{T_{\mathrm{M},1}}\right)^{x_1}\right) \cdot \exp\left(-\left(\frac{2\tau}{T_{\mathrm{M},2}}\right)^{x_2}\right). \quad \text{(S4)}$$

Both approaches attempt to accommodate the presence of two different decoherence mechanisms. There is precedence in the literature to use a SSE to fit Hahn echo decays.[5] To lowest order this represents the assumption that different electron spin populations relax via different mechanisms. Alternatively, a PSE is appropriate if electron spins decohere by two independent but simultaneously operative mechanisms.

Figure S3 compares the fitted stretching exponents and phase memory times from this phenomenological fit. Both d_{18}-TEMPO and p_1TAM were sufficiently fit with a single component stretched exponential. As TEMPO required a second component to reproduce the shape of the experimental decay, the stretching exponents and phase memory times of the nuclear-spin-driven decoherence component of the fits were used (i.e. the one with closer to the predicted ones), as a function of temperature. We see little to no temperature dependence on decoherence behavior of these systems. Neither the phase memory time nor the stretching factor vary significantly over the range of temperatures investigated. The small variations observed in the TEMPO sample are likely due to dynamics of the methyl groups.

3. X-band echo decays

To assess the validity of the model at multiple frequencies, we performed experiments on 10 µM d_{18}-TEMPO in 1:1 (w:w) H_2O:glycerol at X-band (ca. 9.6 GHz) and a temperature of 20 K. Figure S4 shows the resulting experimental echo decay and the simulation. The good match for the X-band experiment with the simulation demonstrates that the model is able to accurately predict decoherence behavior beyond Q-band frequencies.

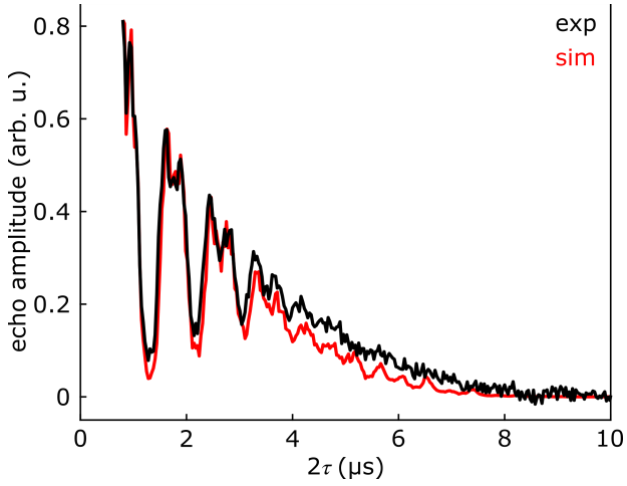

Figure S4. Experimental (black) X-band echo decays of 10 µM d_{18}-TEMPO in 1:1 (w:w) H_2O:glycerol at 20 K and the corresponding MD/CCE model simulations (red). Decays were scaled to have the sample amplitude at the starting point.

4. Simulations

4.1 Molecular Dynamics

Molecular geometries for the decoherence simulations were generated using molecular dynamics (MD) on TEMPO and p_1TAM solvated in water. For TEMPO, we included 5183 water molecules in a cubic box with edge length 55.4 Å, with periodic boundary conditions. For p_1TAM, we used 2717 water molecules in a cubic box with edge length 43.2 Å, with periodic boundary conditions. The radicals were placed at the center of the respective boxes.

Water molecules were modeled with the TIP4P parameterization. To obtain optimized geometries and charges for TEMPO and p_1TAM, we followed Oganesyan[6] and used density functional theory (DFT) with ORCA 4.01, using the B3LYP functional and the SV(P) basis. From the optimized geometries, atomic charges for use in MD were calculated using CHELPG (CHarges from ELectrostatic Potentials using a Grid-based method). The CHELPG charges were then substituted into a topology file generated by CHARMM-GUI.

The MD calculations were performed using GROMACS with the CHARMM36 force field[7] and the particle mesh Ewald method for long-range electrostatics. To generate the initial MD structure, a random distribution of water molecules around the radical was energy minimized. For pre-equilibration, the system was propagated for 100 ps under NVT and then another 100 ps under NPT conditions. From this initial structure, the system was propagated for 25 ns at 300 K in 1 fs steps, followed by 5 ns at 100 K in 1 fs steps, as in the work of Lerbret and Affouard.[8] This approach is used to approximately model the effect of snap freezing the sample. Snapshots were stored every 10 ps. The structure of the last snapshot was converted to PDB format and used as structure input to the spin dynamics simulation.

We chose to perform MD simulations in pure water as opposed to the experimentally used 1:1 (w:w) water:glycerol, since MD simulations on pure water are well calibrated, whereas water-glycerol mixtures are significantly less tested against experiment, particularly in the solid phase needed in the present work. The use of pure water instead of 1:1 (w:w) water:glycerol is not expected to lead to significant errors as the experimental room-temperature proton density of

pure water (110.8 mol L^{-1}) is almost identical to 1:1 (w:w) water:glycerol (111.4 mol L^{-1}).[9] Overall, the error in the MD compared to experiment is likely dominated by errors of predicting correct densities in the solid state.

4.2 Spin Hamiltonian

To model nuclear-spin-driven electron spin decoherence with *N* nuclear spins, we chose the static spin Hamiltonian (in angular-frequency units)

$$\widehat{H}_0 = \mu_{\mathrm{B}} g_{\mathrm{e}} B_0 \hat{S}_z + \sum_{n=1}^{N} \left(-\mu_{\mathrm{N}} g_n B_0 \hat{I}_{z,n} + \hat{S}_z (\boldsymbol{z}^{\mathrm{T}} \boldsymbol{A}_n) \hat{\boldsymbol{I}}_n + \hat{\boldsymbol{I}}_n^{\mathrm{T}} \boldsymbol{P}_n \hat{\boldsymbol{I}}_n \right) + \sum_{m=1}^{N-1} \sum_{n=m+1}^{N} \delta_{g_n, g_m} \hat{\boldsymbol{I}}_m^{\mathrm{T}} \boldsymbol{b}_{m,n} \hat{\boldsymbol{I}}_n \,. \quad \text{(S5)}$$

The first term on the right-hand side of equation S5 is the electron Zeeman interaction. The second term is the sum over all nuclear spins in the system and contains all the terms that depend upon only one nuclear spin: the nuclear Zeeman interaction, the hyperfine interaction, and the nuclear electric-quadrupole couplings. Only the terms that preserve electronic Zeeman energy were kept in the hyperfine coupling, i.e. terms containing $\hat{S}_x$ and $\hat{S}_y$ are neglected. Note that we explicitly retain the pseudosecular terms $\hat{S}_z \hat{I}_x$ and $\hat{S}_z \hat{I}_y$, which are responsible for ESEEM effects. The third term contains all the terms in the Hamiltonian that couple different nuclear spins. The delta function indicates that we only include interactions that conserve Zeeman energy. This is for computational resource management, as the importance of other terms is suppressed by the requirement to conserve energy. For the included couplings, we utilized full coupling tensors. Except for the ^{14}N nitrogen on TEMPO, the hyperfine coupling tensors A_n are calculated using the point-dipole approximation. The nucleus-nucleus coupling tensors $b_{m,n}$ are also calculated using the point-dipole approximation. For ^{14}N on TEMPO, a hyperfine coupling tensor with experimentally determined principal values[10] [-13.9, -13.9, 122.3] MHz and a quadrupole coupling tensor with $e^2 qQ/h$= 3.5 MHz and η = 0.68 were used.[11]

The DFT-optimized geometry for h_{18}-TEMPO was used to calculate d_{18}-TEMPO deuteron quadrupole tensors. The average calculated $e^2 qQ/h$ of 194.5 kHz value was used as an approximation for all CD-deuteron quadrupole tensors. We assumed the quadrupole tensors have axial symmetry; in support of this assumption, the average asymmetry from the ORCA calculation was 0.02.

Microwave pulses were modeled as infinitely short. For a pulse at time t_{p} with flip angle θ_{p}, the Hamiltonian is

$$\widehat{H}_{\mathrm{p}}(t) = \theta_{\mathrm{p}} \delta(t - t_{\mathrm{p}}) \hat{S}_y. \quad \text{(S6)}$$

With these pulses, evolution due to the static Hamiltonian during the pulse is suppressed. The equilibrium density matrix of the system was set equal to $\hat{S}_z$, i.e. the nuclei were treated in the high-temperature limit.

4.3 Spin dynamics

Once the spin system with its spin Hamiltonian was set up, we simulated the two-pulse echo decay experiment by explicit time propagation via integration of the Liouville–von Neumann equation. To deal with the combinatorially large state spaces of the large spin systems, fwe used a home-written implementation of the ensemble Cluster Correlation Expansion (CCE) method.[12,13] The single-sample CCE method has been shown to work for modeling the decoherence of paramagnetic defects and centers in crystals.[14,15] CCE operates in Hilbert space and is based on an expansion of the signal into contributions from nuclear spin clusters of varying sizes. Typically, the expansion converges rapidly for a "bath" of weakly coupled spin-1/2 nuclei and can therefore be truncated. In our experience, the CCE method is more computationally efficient than truncated Liouville space techniques for the problem at hand.

The truncation parameters in the CCE method are illustrated in Figure S5. First, we limit the maximum cluster size (1, 2, 3, etc.). Second, we limit the system size to a sphere of a specific radius r_{Sys} around the electron spin. All spins in the MD box that are outside this sphere are excluded. Third, we only take into account clusters that still form connected graphs (where spins are viewed as vertices and non-zero couplings as edges) when couplings below a chosen cutoff b_{min} are neglected. Like You,[16] we found a neighbor cutoff based on the coupling to be more efficient than based directly on the original distance method;[11] however, we included all clusters that formed connected graphs rather than only those that formed complete graphs. This improved the convergence behavior. To keep the clusterization orientation independent, the condition (in angular frequency units)

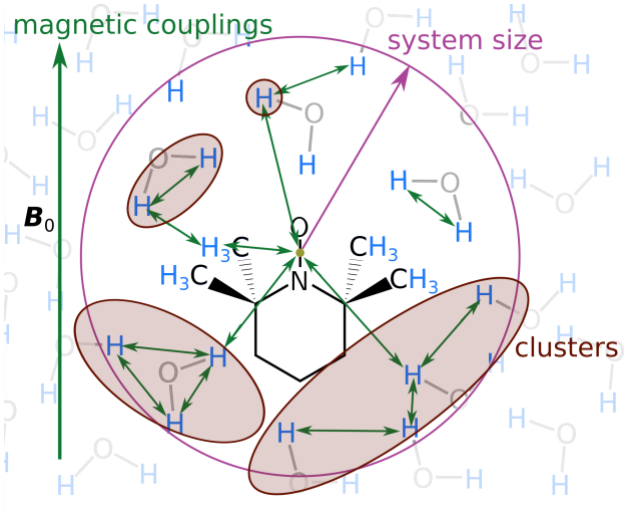

Figure S5. Illustration of the truncation parameters, which are the system size r_{Sys} (purple circle and arrow), the cluster sizes used (rust areas).

$$\frac{\mu_0}{4\pi}\frac{g_m g_n \mu_B}{r_{m,n}^3} > b_{\min} \tag{S7}$$

was used. Since no orientation information is used, this is equivalent to a distance cutoff; the advantage is that every orientation uses the same set of clusters. Fourth, we repeated the second and third steps until both r_{Sys} and $b_{\min}$ are converged. Finally, to reproduce the amorphous nature of the frozen solvent, we averaged the simulations over a finite number of orientations of the applied magnetic field.

To obtain a converged simulated signal as a function of these parameters, we incremented the system size, the neighbor cutoff, and the number of orientations until the condition

$$\left|\frac{T_{\mathrm{M},i} - T_{\mathrm{M},i+1}}{T_{\mathrm{M},i+1}}\right| < \epsilon \tag{S8}$$

was met, where $T_{\mathrm{M},i}$ is defined as the first value of 2τ where the signal dropped to 1/e from 1, for the i^{th} increment. The value of ϵ was chosen at 10^{-3}, to balance accuracy and computational costs. The incrementation scheme for the system size was to increase r_{Sys} by 1 Å each increment. b_{min} was lowered by a factor of $10^{0.2}$ each step. For orientation averaging we increased the number of orientations by using Lebedev grids of increasing size. Table S1 provides the converged parameters for all systems simulated in this work.

Table S1. CCE simulation parameters that gave converged echo decay signals

system	cluster size	system size (Å) r_{Sys}	neighbor cutoff (Hz) b_{min}	# of orientations	# of nuclear spins	# of 2-clusters
TEMPO	2	17	100	170	1442	165750
d_{18}-TEMPO	2	15	630	170	996	20607
p_1TAM	2	18	100	14	1639	173489
d_{18}-TEMPO (X-band)	2	17	63	74	1442	231754

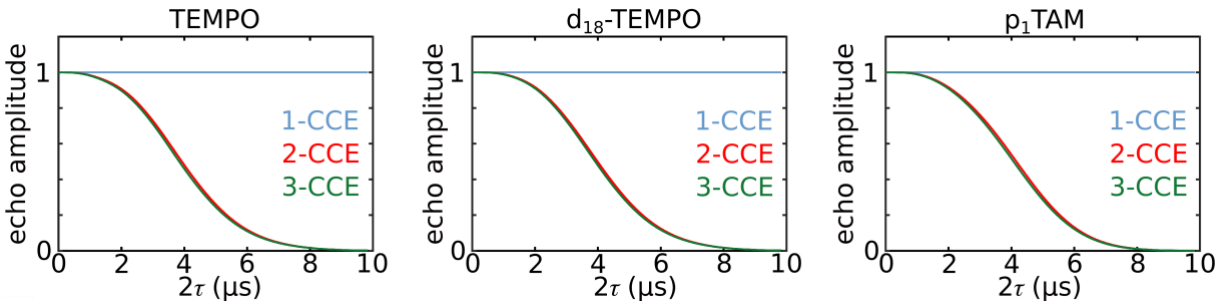

Figure S6. The effect of cluster size on simulated decoherence behavior for the three systems in this study. These decoherence curves were calculated for a single orientation, and at the parameters that give at least 90% the converged T_{M}. The Hamiltonians used here do not contain pseudo-secular hyperfine terms or nuclear quadrupole coupling but is otherwise given in equation S5. The difference between truncating at cluster size 1 versus size 2 is significant, but the 3-cluster correction is small.

An important convergence parameter is at which cluster size to truncate the CCE product. Figure S6 show a comparison of simulations truncated at sizes 1, 2, and 3 (using a single orientation with the system size and neighbor cutoff that gave a least 90% the converged 2-cluster CCE T_{M}). The signal shows no decay with cluster size 1, but an almost converged decay with cluster size 2. This shows that pairs of nuclei are responsible for decoherence. The signals change insignificantly between cluster size 2 and 3. This is consistent with previous findings that simulation of sequences with odd π pulse parity, like the Hahn echo experiment, are mostly contained by the 2-cluster CCE size.[8] Therefore, all our calculations are truncated at cluster size 2.

5. Decoherence due to individual nuclei

To assess the effect of an individual nucleus i on electron decoherence, we compared the 1/e decay points of simulated Hahn echo decays of the full system and the system upon removal of nucleus i. This yields a small change, $\Delta T_{\mathrm{M},i}$, as is illustrated in Fig. S7. This quantity is the amount by which T_{M} would increase if magnetic nucleus i were replaced by a nonmagnetic isotope. Fig. S8 illustrates the resulting $\Delta T_{\mathrm{M},i}$ for all nuclei in all three systems employed in this work.

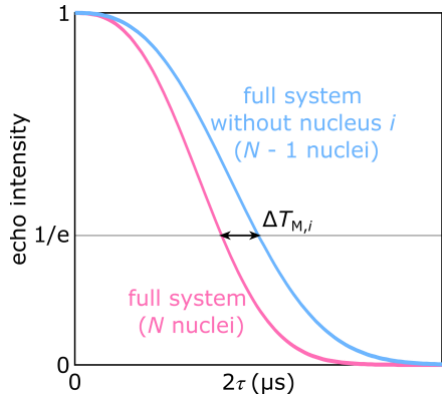

Figure S7. Schematic illustration of the approach that quantifies the effect of individual nuclei on decoherence. The removal of one nucleus prolongs the decoherence time.

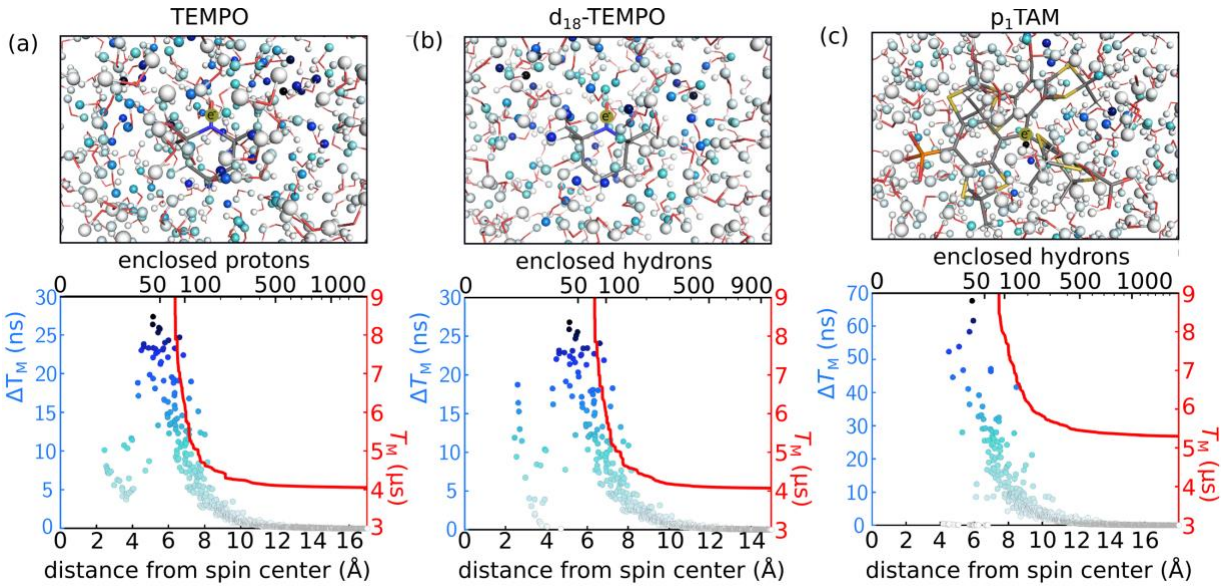

Figure S8. (top) Decoherence time reduction map for (a) h_{18}-TEMPO, (b) d_{18}-TEMPO, and (c) p_1TAM (all in H_2O) illustrating how much individual hydrons (protons, deuterons) contribute to the loss of electronic coherence. Darker blue indicates a higher level of influence on decoherence, using the color scale shown in (b). (bottom) The value of ΔT_{M} (left axis and blue dots) indicates the extension of the decoherence timescale resulting from removing a given hydron. The right axis with the red curve shows the overall T_{M} calculated by including only nuclei within the distance to the electron given by the abscissa in the CCE simulation.

6. References

(1) Dhimitruka, I.; Bobko, A. A.; Eubank, T. D.; Komarov, D. A.; Khramtsov, V. V; Davis, D. M. Phosphonated Trityl Probes for Concurrent in Vivo Tissue Oxygen and PH Monitoring Using Electron Paramagnetic Resonance-Based Techniques. *J. Am. Chem. Soc.* **2013**, *135*, 5904–5910. https://doi.org/10.1021/ja401572r.

(2) Klauder, J. R.; Anderson, P. W. Spectral Diffusion Decay in Spin Resonance Experiments.

Phys. Rev. **1962**, *125* (3), 912–932. https://doi.org/10.1103/PhysRev.125.912.
(3) Salikhov, K. M.; Dzuba, S. A.; Raitsimring, A. M. The Theory of Electron Spin-Echo Signal Decay Resulting from Dipole-Dipole Interactions between Paramagnetic Centers in Solids. *J. Magn. Reson.* **1981**, *42*, 255–276. https://doi.org/10.1016/0022-2364(81)90216-X.
(4) Zecevic, A.; Eaton, G. R.; Eaton, S. S.; Lindgren, M. Dephasing of Electron Spin Echoes for Nitroxyl Radicals in Glassy Solvents by Non-Methyl and Methyl Protons. *Mol. Phys.* **1998**, *95* (6), 1255–1263. https://doi.org/10.1080/00268979809483256.
(5) Soetbeer, J.; Hü, M.; Godt, A.; Polyhach, Y.; Jeschke, G. Dynamical Decoupling of Nitroxides in O-Terphenyl: A Study of Temperature, Deuteration and Concentration Effects †. *Phys. Chem. Chem. Phys* **2018**, *20*, 1615–1628. https://doi.org/10.1039/c7cp07074h.
(6) Oganesyan, V. S. A General Approach for Prediction of Motional EPR Spectra from Molecular Dynamics (MD) Simulations: Application to Spin Labelled Protein. *Phys. Chem. Chem. Phys* **2011**, *13*, 4724–4737. https://doi.org/10.1039/c0cp01068e.
(7) Best, R. B.; Zhu, X.; Shim, J.; Lopes, P. E. M.; Mittal, J.; Feig, M.; Mackerell, A. D. Optimization of the Additive CHARMM All-Atom Protein Force Field Targeting Improved Sampling of the Backbone φ, ψ and Side-Chain χ 1 and χ 2 Dihedral Angles. *J. Chem. Theory Comput.* **2012**, *8*, 3257–3273. https://doi.org/10.1021/ct300400x.
(8) Lerbret, A.; Frédé, F.; Affouard, F. Molecular Packing, Hydrogen Bonding, and Fast Dynamics in Lysozyme/Trehalose/Glycerol and Trehalose/Glycerol Glasses at Low Hydration. *J. Phys. Chem. B* **2017**, *121*, 9437−9451. https://doi.org/10.1021/acs.jpcb.7b07082.
(9) *Physical Properties of Glycerine and Its Solutions*; Glyerince Producers' Association: New York, NY, 1963.
(10) Owenius, R.; Engström, M.; Lindgren, M.; Huber, M. Influence of Solvent Polarity and Hydrogen Bonding on the EPR Parameters of a Nitroxide Spin Label Studied by 9-GHz and 95-GHz EPR Spectroscopy and DFT Calculations. *J. Phys. Chem. A* **2001**, *105*, 10967–10977. https://doi.org/10.1021/jp0116914.
(11) Oliveira, M. De; Knitsch, R.; Sajid, M.; Stute, A.; Elmer, L.-M.; Kehr, G.; Erker, G.; Magon, C. J.; Jeschke, G.; Eckert, H. Aminoxyl Radicals of B/P Frustrated Lewis Pairs: Refinement of the Spin-Hamiltonian Parameters by Field-and Temperature-Dependent Pulsed EPR Spectroscopy. *PLoS One* **2016**, *11* (6), e0157944. https://doi.org/10.1371/journal.pone.0157944.
(12) Yang, W.; Liu, R. B. Quantum Many-Body Theory for Qubit Decoherence in a Finite-Size Spin Bath. *AIP Conf. Proc.* **2008**, *1074*, 68–71. https://doi.org/10.1063/1.3037140.
(13) Yang, W.; Liu, R.-B. Quantum Many-Body Theory of Qubit Decoherence in a Finite-Size Spin Bath. II. Ensemble Dynamics. *Phys. Rev. B* **2009**, *79* (11). https://doi.org/https://doi.org/10.1103/PhysRevB.79.115320.
(14) Lenz, S.; Bader, K.; Bamberger, H.; Van Slageren, J. Quantitative Prediction of Nuclear-Spin-Diffusion- Limited Coherence Times of Molecular Quantum Bits Based on Copper(II). *ChemComm* **2017**, *53* (53), 4477–4480. https://doi.org/10.1039/c6cc07813c.
(15) Ma, W. L.; Wolfowicz, G.; Zhao, N.; Li, S. S.; Morton, J. J. L.; Liu, R. B. Uncovering Many-Body Correlations in Nanoscale Nuclear Spin Baths by Central Spin Decoherence. *Nat. Commun.* **2014**, *5*, 1–9. https://doi.org/10.1038/ncomms5822.

(16) You, J.; Carić, D.; Rakvin, B.; Štefanić, Z.; Užarević, K.; Kveder, M. Matrix Material Structure Dependence of the Embedded Electron Spin Decoherence. *J. Chem. Phys* **2019**, *150*, 164124. https://doi.org/10.1063/1.5090215.

]]]